

# Nanoscale resolution immersion scanning thermal microscopy

*Peter D. Tovee and Oleg V. Kolosov.*

Physics Department, Lancaster University, Lancaster, LA1 3BE, UK.

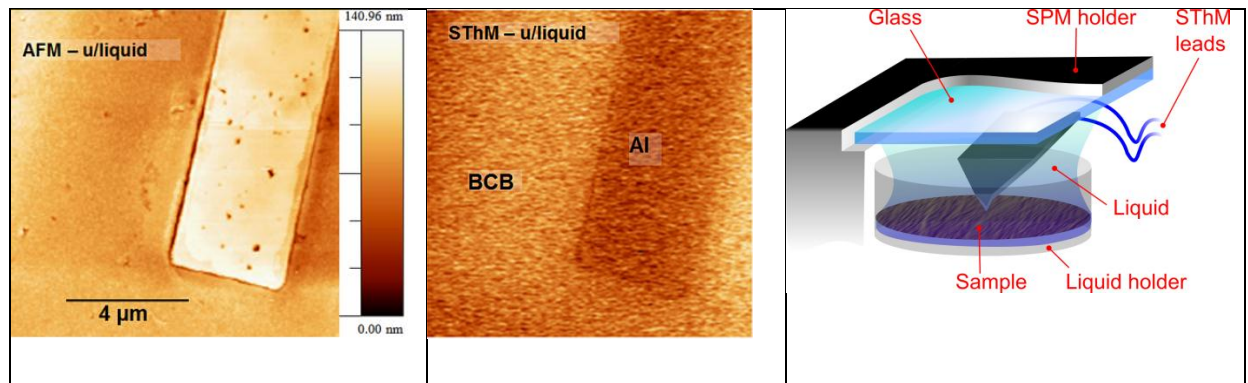
Corresponding Author; o.kolosov@lancaster.ac.uk

Keywords; scanning thermal microscopy, nanoscale imaging, liquid environment, immersion, graphene

Abstract:

Nanoscale thermal properties are becoming of extreme importance for modern electronic circuits that dissipate increasing power on the length scale of few tens of nanometers, and for chemical and physical properties sensors and biosensors using nanoscale sized features. While Scanning Thermal Microscopy (SThM) is known for its ability to probe thermal properties and heat generation with nanoscale resolution, until today it was perceived impossible to use it in the liquid environment due to dominating direct heat exchange between micro-fabricated thermal probe and surrounding liquid that would deteriorate spatial resolution. Nonetheless, our theoretical analysis of SThM in liquids showed that for certain design of SThM probe with resistive heater located near the probe tip, their thermal signal is only moderately affected, by less than 50 % on immersion in a dodecane environment. More significantly, its spatial resolution, surprisingly, would remain practically unaffected, and the thermal contact between the tip apex and the studied sample would be beneficially improved. Our experimental trials of such immersion SThM, or iSThM, were fully successful and here we report for the first time

nanoscale SThM measurements of thermal conductivity of Ultra Large Scale Integration polymer-ceramic-metal interconnects with the spatial thermal resolution down to 50 nm. Further studies of heat transport in nanoscale graphite flakes in iSThM suggested, that highly anisotropic thermal conductivity in graphene layers may play significant role in the nanoscale thermal transport in liquid environment. New iSThM opens a wide range of applications from non-contact measurements of thermal transport in semiconductor devices to exploring graphene energy storage, catalytic reactions and heat generation in biological systems.



Since its invention, scanning probe microscopy (SPM)<sup>1,2</sup> became an indispensable tool in modern nanotechnology, allowing mapping of material surfaces with nanoscale resolution,<sup>3</sup> direct exploration of structure of nanoscale devices,<sup>4,5</sup> imaging of individual protein molecules<sup>6</sup> and atoms, including intramolecular electronic structure.<sup>7</sup> A significant advantage of SPM approaches is their ability to sense diverse physical and chemical properties of such structures with nanometer resolution,<sup>8-11</sup> including operation in various environments,<sup>12-14</sup> supporting and initiating novel nanotechnology developments. Among properties explored, nanoscale measurements of temperature<sup>15,16</sup>, heat generation and nanoscale heat propagation are of increasing importance encouraged by continuous decrease of size of semiconductor devices with concurrent increase of processing power.<sup>17</sup> While Scanning Thermal Microscopy (SThM)<sup>18-22</sup> that uses self-thermal sensors integrated with the sharp tip brought into thermal contact with the studied sample, addresses some of these demands, perhaps the major obstacle for SThM advance is the weak thermal coupling between sensor and the sample,<sup>23</sup> that additionally, fluctuates due to local variations of sample nanoscale geometry, hence often drastically reducing SThM performance.

It would be very tempting to use liquid immersion in SThM to significantly improve both the thermal contact between the probe tip and the sample, as well as its stability, in an approach somewhat similar to one used in ultrasonic imaging where gel is used to achieve better acoustic coupling<sup>24</sup> or optical immersion where light reflection, refraction and scattering at the interfaces are minimized.<sup>25</sup> In liquid fluorescence thermometry so far showed only micrometer scale spatial resolution<sup>26</sup> and being a passive method, would not allow measurements of local thermal conductivities. Immersion SThM probe measurements, if available, would be also of extreme interest for biotechnology, where the heat of intermolecular interactions can help to explore functioning of molecular motors<sup>27</sup> and energy transfer in photosynthesis,<sup>28</sup> as well as in chemistry in studies of nanoscale catalysts.<sup>29</sup> Unfortunately until now such underliquid operation of SThM has been considered all but impossible<sup>23</sup> due to the potentially overwhelming direct heat dissipation from the heated sensor into the surrounding liquid, that would lead to degradation of lateral resolution. To our knowledge, there is so far no publication reporting such approach and measurements.

Notwithstanding the rationale described above, in this paper we simulated such immersion SThM, or iSThM,<sup>30</sup> based on a widely used design of a SThM probe that is fully immersed in a

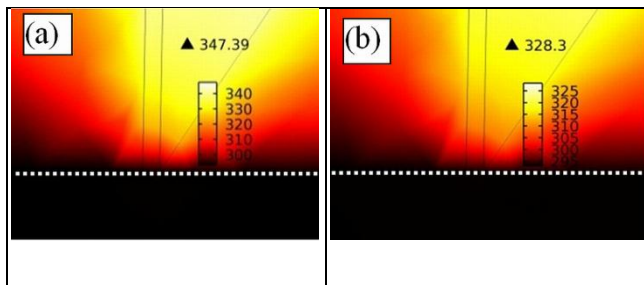
liquid. We found, surprisingly, that such measurements would not be qualitatively different from the operation in air or vacuum environment reported elsewhere.<sup>31</sup> Furthermore, we then realized such iSThM and demonstrated its capabilities on the system of polymer-ceramic-metal Ultra Large Scale Integration (ULSI) interconnects, as well as for 30 nm thick graphite flake on Si substrate, showing thermal mapping with 50 nm lateral resolution, comparing obtained results with the simulations.

## RESULTS AND DISCUSSION

SThM<sup>18,19,23,32,33</sup> is similar in many ways to the atomic force microscope (AFM).<sup>2</sup> In both, the tip is scanned across the sample surface in a raster way following its topography using a feedback loop that maintains a constant tip-surface force. The tip is Joule heated by passing a current through a resistive element near the tip apex. The probe design can vary from Wollaston wire (WW)<sup>34</sup> to Si<sub>3</sub>N<sub>4</sub> microfabricated thermal probe with a thin Pd track (SP) as the tip heater<sup>35</sup> (Kelvin Nanotechnology) to microfabricated doped Si probe (Anasys Instruments)<sup>21</sup> (DS) and thermocouple junction probe<sup>18,22</sup>. The thermal resolution of the WW probe is about 1  $\mu$ m whereas for microfabricated DS and SP probes it can be well below 100 nm.<sup>31,36,37</sup> As the tip is brought in contact with the surface the heat flows into the sample cooling the tip. Using a Maxwell bridge or similar measurement setup<sup>30</sup> (see Supporting Materials) the well-defined power can be applied to the sensor generating Joule heat, whereas the tip temperature can be measured simultaneously. As the tip is scanned across the sample, monitoring these values allows us to create a thermal image of the sample and to evaluate its local thermal resistance.  
23,31,38

**Motivation and feasibility of SThM in liquid environments.** While the role of liquid film between the SThM tip apex is known to be essential<sup>23,39-41</sup> up to now there were no reports on SThM probes fully immersed in the liquid. Such liquid immersion could provide improved and stable thermal contact between the tip and the surface, compared to in-air or vacuum environment. Also, due to efficient heat transfer through liquid, it might be possible to perform truly non-contact scanning with the tip-surface separated by few nm gap, while retaining both nanoscale resolution and thermal sensitivity. For biomedical applications, SThM underliquid operation will allow handling of delicate biological samples such as used in other SPM methods,<sup>42-44</sup> whereas in industrial applications, it may open pathways for exploring nanoscale thermal phenomena in power batteries and fuel cells.<sup>29</sup>

So far SThM operation both in air and vacuum was demonstrated, with vacuum helping to eliminate heat dissipation through air.<sup>22,37,31</sup> At first glance, the direct heat dissipation from SThM probe to the surrounding liquid might result in the complete loss of sensitivity to the local sample thermal properties. Nevertheless, our preliminary simulations of SThM response using experimentally verified finite element analysis (FEA) model of the probe<sup>30</sup> for a widely used SP probe showed only a moderate decrease in thermal signal (Figure 1) while replacing air with dodecane. It can be seen that the highest temperature of SThM sensor is only slightly lower in liquid (35 degrees above ambient environment at 293 K) compared with air (54 degrees). More significantly, the spatial distribution of the temperature was strikingly similar in air and liquid (Figure 1a, b) and the heat “plum” was located along the SThM tip rather than widely spread in the surrounding liquid (Figure 1c), leading to lateral resolution of the probe not very different from one operating in air or vacuum. At the same time, simulation of the behavior of the DS probe (with heater positioned at the end of cantilever far from the tip apex) did indicate significant deterioration of both thermal spatial resolution and sensitivity. The dodecane was selected as it is a low-volatility liquid with intermediate thermal conductivity and was tested to be non-corrosive to the particular sensor. Finally, our simulations showed that SThM “hovering” above sample surface at 25 nm distance in liquid would still provide reasonable thermal contact to the sample (with sensor temperatures readings close to the tip in direct contact with the sample), whereas in air these readings are much more diverging (see Table 1 in Figure 1d and Methods).



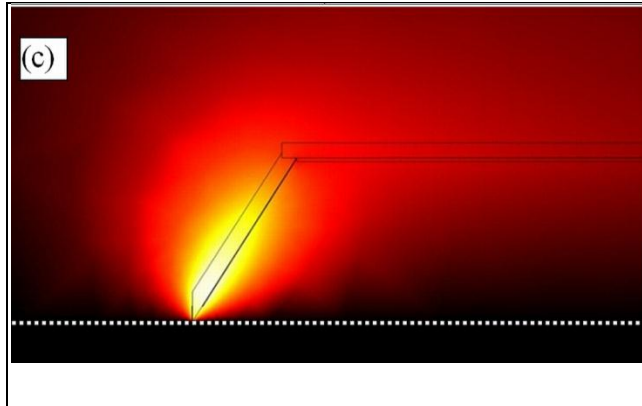


Figure 1. Finite elements analysis (FEA) simulations of SP SThM tip in (a) contact with Si in air and (b) contact with Si in dodecane.  $T_{\max}$  – is the maximal temperature of the heater with respect to ambient temperature of 293 K, dotted lines indicate the sample surface. (c) Wider view of temperature distribution of SThM probe in contact with Si in dodecane.

Table 1. Sensor temperature change  $\Delta T$  for tip hovering above the Si sample, in air and dodecane environments.

$\Delta z$ , nm	Air/ liquid	$\Delta T$ (mK)
$\Delta z = 0$ nm	Air	0
(contact)		
$\Delta z = 25$ nm	Air	45
("hovering" non-contact)		
$\Delta z = 200$ nm (non-contact)	Air	99

$\Delta z = 0$  nm Liquid 0  
(contact)

---

$\Delta z = 25$  nm Liquid 9  
("hovering" non-  
contact)

---

$\Delta z = 200$  nm (non- Liquid 51  
contact)

---

\*Given that MFP in air of 50 nm,  
correction value for  $\Delta T$  for "hovering" in  
air at  $\Delta z = 25$  nm would further bring it  
closer to "non-contact" value of 99 mK

---

We then created a simplified analytical model of the SThM probe in order to estimate the influence of the heat loss to the environment. First, it is possible to consider that the base of the thin triangular shaped  $\text{Si}_3\text{N}_4$  probe of width  $w_c$  is effectively thermally anchored to the ambient temperature via thick highly thermally conductive Au leads<sup>30</sup>. Secondly, the resistive heater that is also a temperature sensing element is evenly distributed along the length of the probe  $L_c$ . Finally, in first approximation, the heat transfer to the base of the probe is directed along the  $\text{Si}_3\text{N}_4$  sheet of thickness  $t_c$ , whereas heat loss to the environment is predominantly normal to this sheet. The thermal resistance of the probe to the base can then be estimated as  $R_b = \Delta T/Q = (t_c k w_c / L_c)^{-1}$  where  $k$  is thermal conductivity of the probe material,  $\Delta T$  is probe temperature increase and  $Q$  is Joule heat generated in the probe. The thermal resistance of the probe to the ambient media (air or liquid) can then be estimated  $R_m = \sqrt{1 - w_c / (2\pi L_c)} / 2\pi k_m L$  where  $k_m$  is thermal conductivity of the media. As these thermal resistance act in parallel, the total thermal resistance  $R_t$  is determined<sup>23,31</sup> as  $R_t = R_b R_m / (R_b + R_m)$ . Substituting values for our probe ( $L_c = 10 \mu\text{m}$ , thermal conductivity for sputtered  $\text{Si}_3\text{N}_4$   $k_{\text{Si}_3\text{N}_4} \approx 4 \text{ W/mK}$ ,  $k_{\text{air}} = 0.025 \text{ W/mK}$ ,  $k_{\text{dodecane}} = 0.14 \text{ W/mK}$ ) we obtain the estimate of the thermal resistance of the tapered end of the SThM probe as  $1.0 \times 10^5 \text{ K/W}$  in the air and in dodecane of  $0.56 \times 10^5 \text{ K/W}$ . The thermal resistance for dodecane is approximately twice lower than for an air environment due to dodecane's higher thermal conductivity, accounting for approximately 50 % drop of the probe

signal, in line with the FEA analysis of the probe and which should still provide sufficient response for SThM measurements (see also Supporting Material for details).

**Experimental realization of iSThM.** Our iSThM was based on an AFM (Bruker multi-mode, with Nanoscope III controller) modified for use with liquids and SThM (see Methods and Supporting Materials). For working under liquid a special PTFE holder was designed to contain the liquid with width sufficient to accommodate thermal cantilevers and connecting leads. A cantilever holder was additionally modified with glass window to create a flat glass-liquid interface for AFM laser beam monitoring cantilever deflection (Figure 2a).

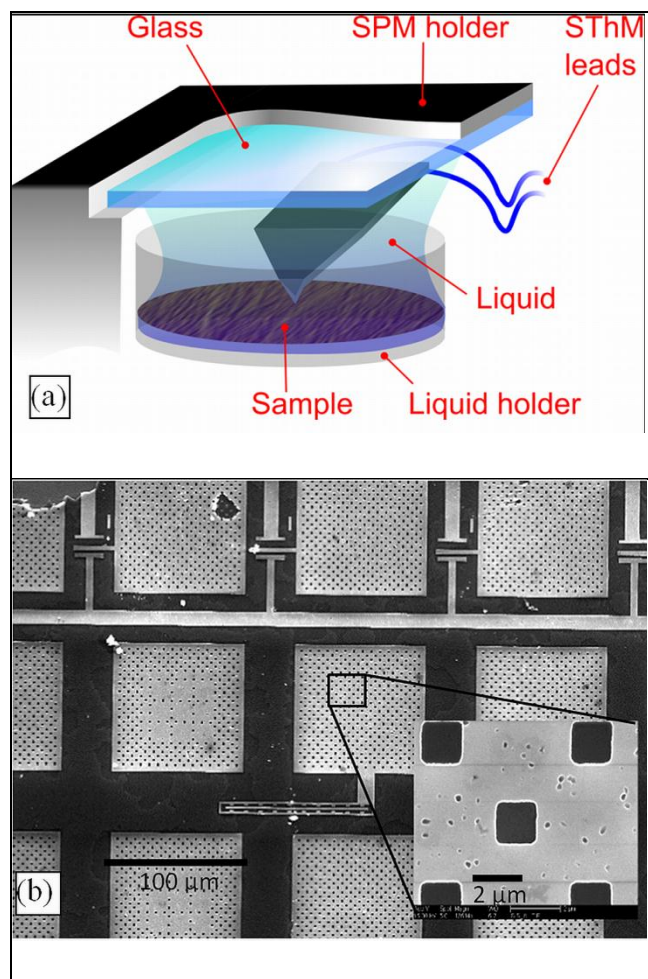


Figure 2. (a) Diagram of AFM holder modified for use for under liquid SThM with glass plate to form a flat interface for laser beam monitoring the probe deflection, and a PTFE holder for the



immersion liquid and a sample. (b) SEM image of Al - BCB (bensocyclobutene) polymer interconnects<sup>45</sup>; inset - higher magnification. Dark areas are the BCB polymer with the lighter grey areas the Al tracks with small holes at the grain boundaries clearly visible.

To study the feasibility and performance of iSThM we used a test structure of chemo-mechanically polished damascene ultra large scale integration (ULSI) interconnects with Al tracks in a benzocyclobutene (BCB) polymer matrix on a Si wafer<sup>45</sup> (Figure 2b). Heat transport in such nanostructures is of significant concern as these tracks in a real device carry significant amount of current and their overheating would adversely affect the stability of the ULSI device. Such structure also has a high (Al) and relatively low (BCB) thermal conductivity materials side-by-side with a well-defined boundaries that would allow to estimate both thermal sensitivity and resolution of SThM. The same sample was scanned first in air and then in dodecane to ensure no dodecane contamination has been left behind. SThM images in Figure 3 were obtained with constant power applied to the sensor and resulting temperature recorded via measuring resistance variations of the sensor (see Methods and Supporting Materials). The higher heat transfer to the sample results in the lower sensor temperature and darker areas in the image; scan speed of about 0.4 Hz was used to produce clear thermal images. The air SThM image (Figure 3b) clearly shows that the Al interconnects produce better heat dissipation from the tip corresponding to lower thermal resistance. This is consistent with the higher thermal conductivity for Al,  $k_{Al} = 200$  W/mK compared to BCB,  $k_{BCB} = 29$  W/mK. The topographical variations (as high as 120-140 nm) seem to provide no artifacts in thermal image, whereas voids in Al filled with air seem to create a barrier to the heat transport (increase in thermal resistance) resulting in “hotter” bright areas in SThM image.

iSThM was able to produce very similar thermal contrast, of somewhat lower signal-to-noise ratio, with areas of Al interconnects revealing better heat dissipation (Figure 3d). It is interesting to note that in iSThM voids in Al did not produce significant increase in thermal resistance that would be consistent with the fact that they are filled with heat conducting liquid rather than air.

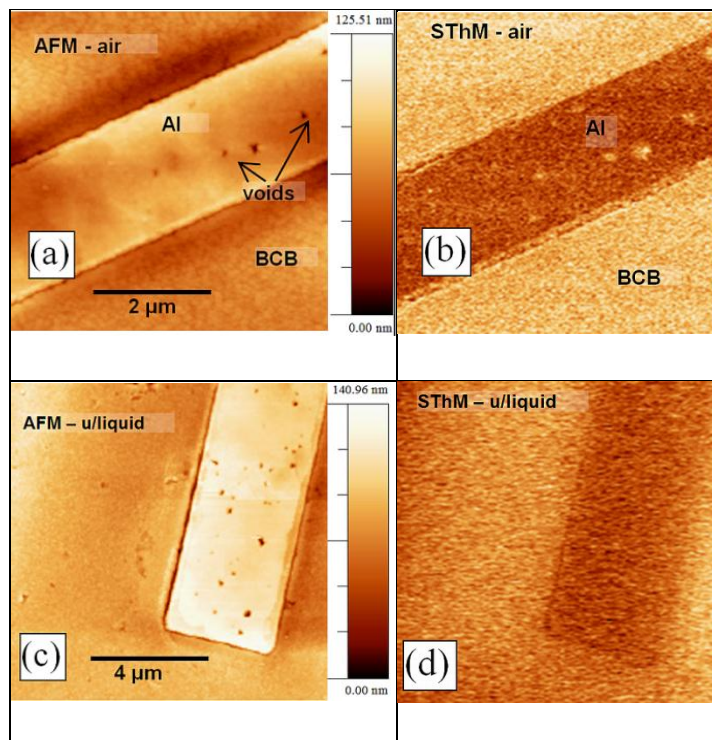


Figure 3. SThM images of Al - BCB polymer interconnects sample in air showing (a) topographic height and (b) thermal signal. c, d) iSThM scans showing (c) the height image and (d) and thermal signal of the same sample fully immersed in dodecane. For the constant heat generated by the probe, lower thermal resistance (higher thermal conductivity) results in the lower temperature of the sensor, and therefore darker contrast. Scale bars showing the height are situated next to (a) and (c). The darker areas in thermal images (b) and (d) are the Al tracks reflecting the higher thermal conductivity of Al.

In order to further analyze the performance of iSThM, we captured thermal signal and mechanical deflection of SThM sensor (proportional to force between the sample and SThM tip) as the tip approached the sample. Approach curves were carried out over Si sample with slow 0.01 Hz approach-retract rate. The signal decreases as expected as the tip approaches the surface

since the heat is conducted to the sample cooling the probe. Once the solid-solid contact is established, the thermal signal remains constant even the force continue increasing, as it has been reported elsewhere.<sup>41</sup>

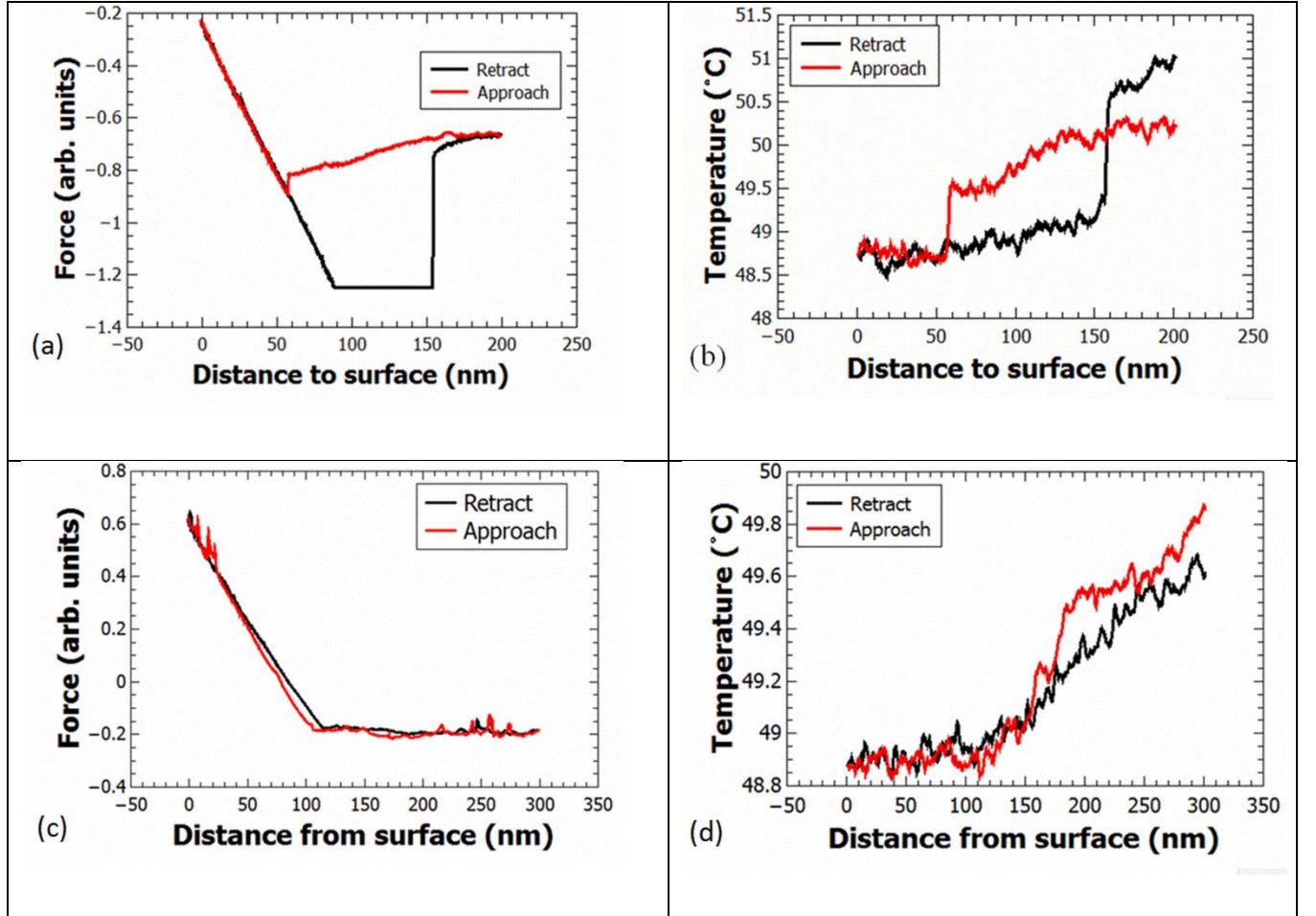


Figure 4. Experimental SThM approach-retract curves for Si sample. (a) Is force and (b) is SThM signal in air compared with (c) force and (d) SThM signal in dodecane (approach-retract rate was 0.01 Hz). Whereas there is a snap-in of cantilever in air (a) that is reflected in the jump in SThM response (b), there is neither force (c) nor observable SThM signal discontinuity while operating in liquid (d).

It is essential to note that in liquid there was no snap-in of tip to the sample due to attractive forces<sup>46</sup> that generally accompanies any AFM in-air measurements, that would allow to easily realize “hovering” of the SThM tip apex in the vicinity of the sample therefore preserving thermal contact between them, while performing non-contact imaging with, *e.g.*, shear force

feedback. From Figure 4 it is clear that at longer distances both in air and in dodecane SThM signal depends on the distance between sample and the apex of the probe tip.

In addition to metal-polymer pair we have also obtained thermal conductivity maps of anisotropic graphite nano-flake ( $k_{\parallel-Gr-plane} = 2000 \text{ W/mK}$   $k_{\perp-Gr-plane} = 2 \text{ W/mK}$ ) of approximately 30 nm thickness on Si substrate ( $k_{Si} = 130 \text{ W/m K}$ ), comparing air and iSThM images (Figure 5).

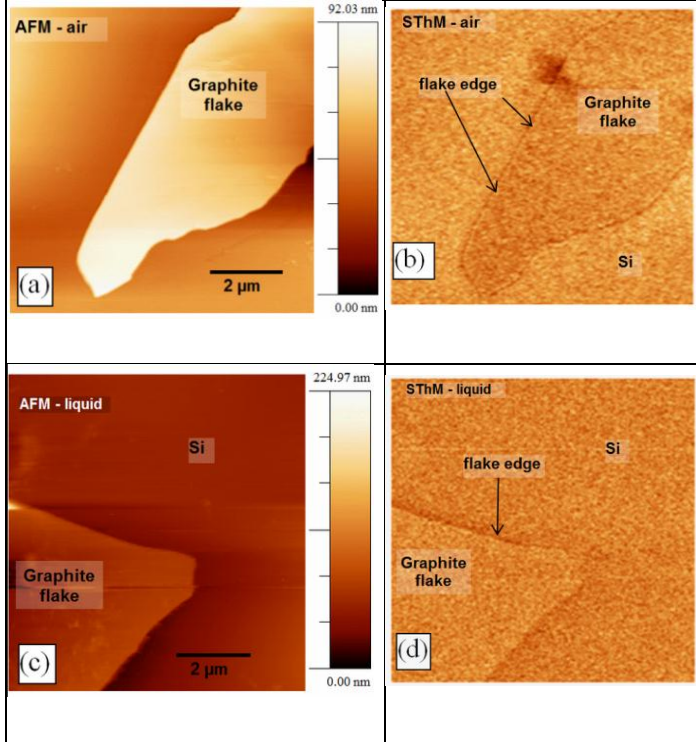
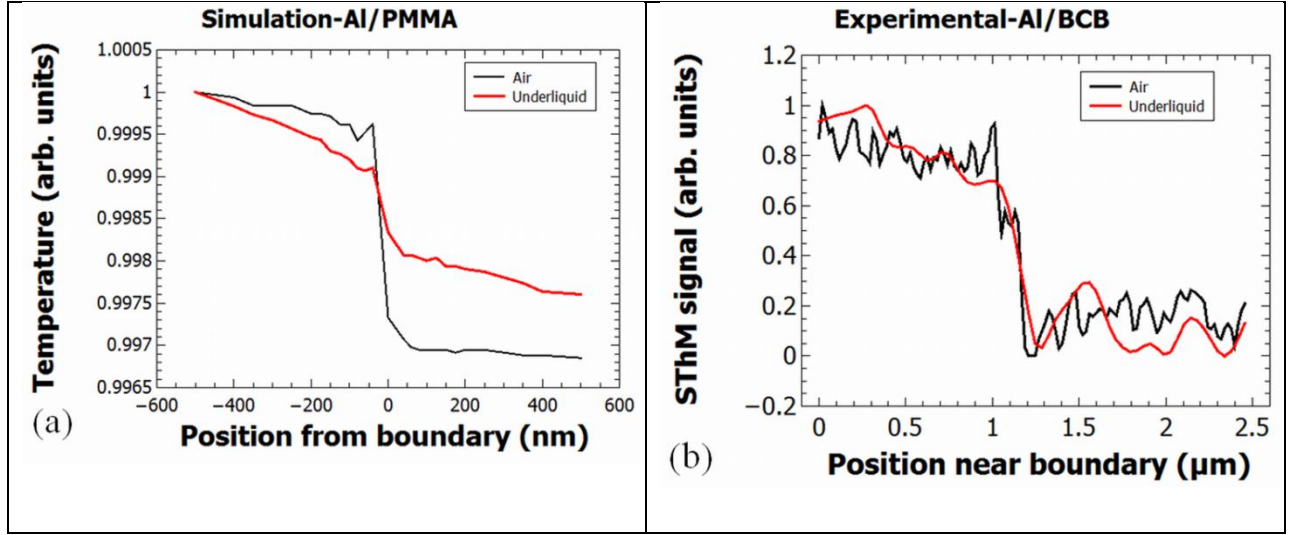


Figure 5. Thin graphite flake in air and in iSThM. Air topography (a) and SThM (b) images; c) topography and iSThM (d) images of similar flake in dodecane. The heat flux normal to graphene layers is similar to one of Si, whereas side surface of the flake provide a better heat dissipation. Graphite flake thickness; (a) air 35-45 nm and (c) liquid 40-50 nm.

The SThM signal on graphite nano-flake (and therefore heat flux normal to the graphite flake surface) was similar to one of Si both in air and iSThM. That can be explained by the relatively low heat conductivity of graphite normally to the atomic planes<sup>46</sup> as well as increased interface resistance.<sup>47</sup> At the same time, SThM signal at the flake edge revealed consistently higher

thermal flux in both air and liquid environments (Figure 5c, d). Although solid-solid contact area would increase at the flake edge, by comparison with ULSI interconnects, it was possible to rule out the direct topography influence on our probe (topographical variations in ULSI of 100 nm, significantly exceeded ones for graphite at 30 nm) attributing this phenomenon to mainly resulting from the extreme in-plane thermal conductivity of graphene layers contacted by the side of SThM probe.<sup>46</sup> As this effect was visible in both air and iSThM, it suggests the possibility to explore anisotropy of phonon propagation in liquid environment.<sup>48</sup>

In order to explore the clearly different nature of thermal contrast in ULSI interconnects of Al vs BCB, and of graphite flake on Si, we have performed FEA simulations of SThM line scans across Al/BCB boundary and graphite/Si edge and compared them with the experimentally measured line scans. Given that mean free path for thermal transfer in liquids is on the order of 10 nm whereas distances and probe dimensions we are considering are of 50 nm or above, such approach was deemed appropriate<sup>49,50</sup>.





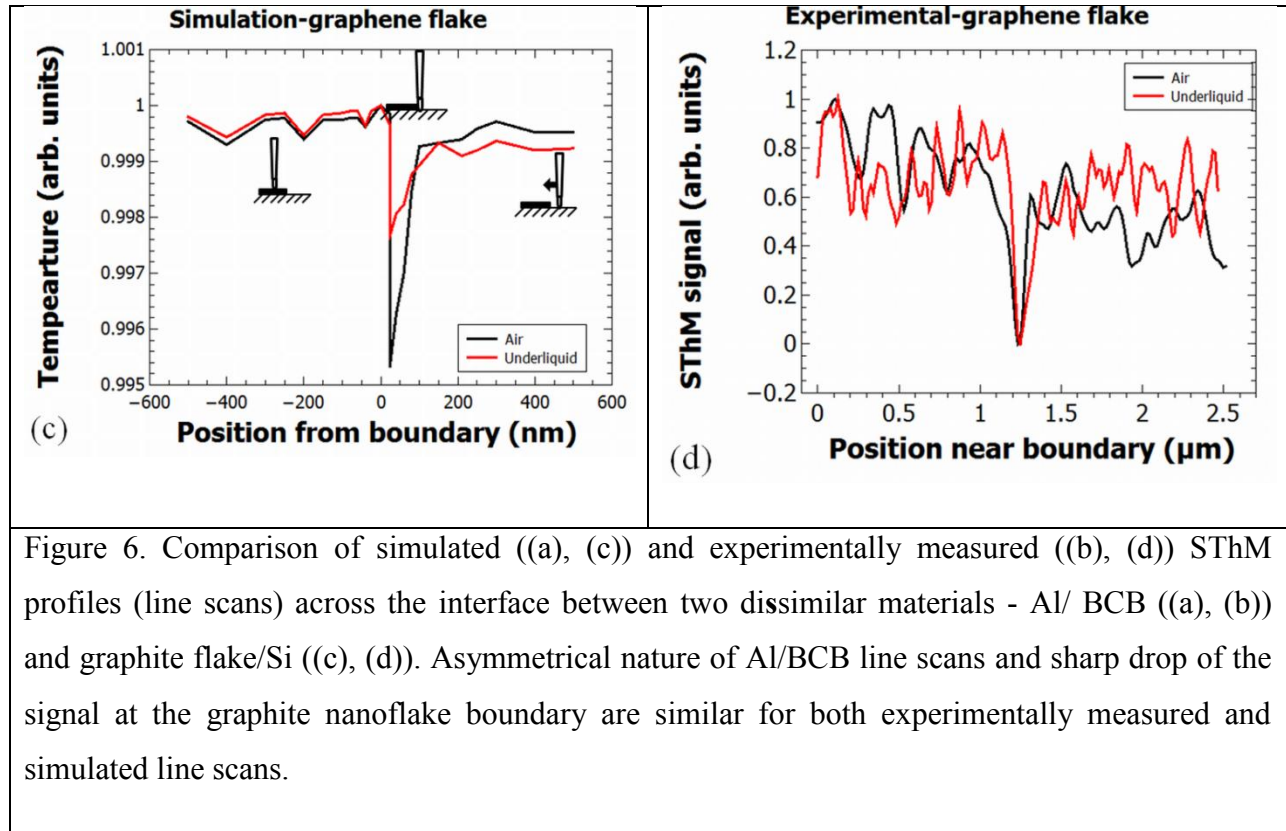


Figure 6. Comparison of simulated ((a), (c)) and experimentally measured ((b), (d)) SThM profiles (line scans) across the interface between two dissimilar materials - Al/ BCB ((a), (b)) and graphite flake/Si ((c), (d)). Asymmetrical nature of Al/BCB line scans and sharp drop of the signal at the graphite nanoflake boundary are similar for both experimentally measured and simulated line scans.

Results of our simulations show that the SThM signal on the Al – polymer boundary (Figure 6a) does change appreciably over approximately 50 nm lateral distance, in good correlation with the experimental results (Figure 6b). The experimentally measured and simulated thermal signals for Al are significantly lower compared to the polymer, which is explained by the large difference in thermal conductivity between Al and BCB. In dodecane this transition is smaller in amplitude however still provides similar lateral resolution of about 50 nm. For graphite nanoflake, the simulation provided additional support to our experimental finding, suggesting a drop of the SThM signal at the very edge of the flake, and small difference of SThM signal on the top of the flake compared with Si substrate. This drop is more significant in air, but is still observable in iSThM in liquid. Simulations for both isotropic and anisotropic graphite models showed somewhat similar behavior, but the temperature drop for side contact with the isotropic case was notably lower than for the anisotropic one, as expected for higher thermal conductivity in-graphene plane.

## CONCLUSION

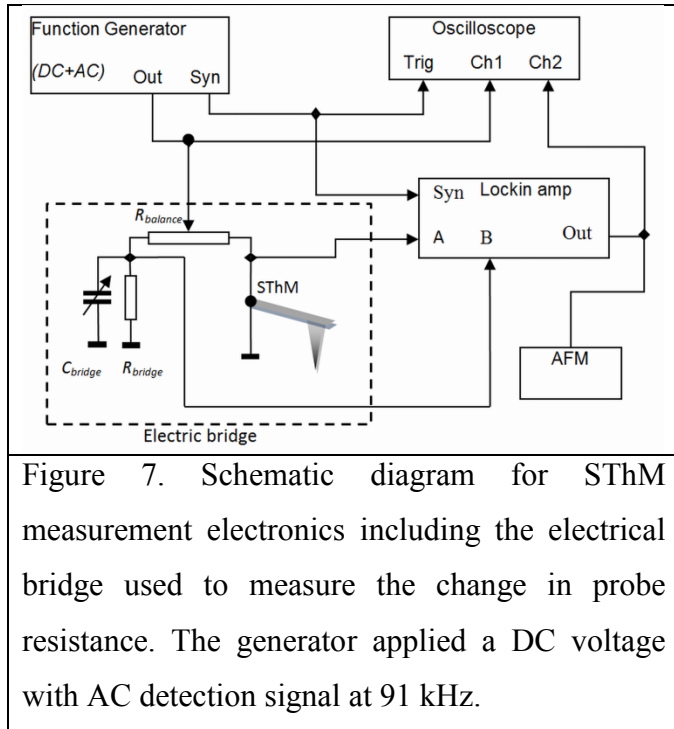
In conclusion, we have demonstrated for the first time that SThM in fully immersed liquid environment is fully viable and can achieve nanoscale thermal resolution in samples with spatially inhomogeneous thermal conductivity. New immersion SThM (iSThM) allowed thermal mapping of ultra large scale integration (ULSI) Al - low- $k$  BCB polymer interconnects and graphite nanoflakes on Si substrate demonstrating lateral resolution of about 50 nm. The probe thermal response was shown to be in good qualitative agreement with analytical estimates as well as finite elements simulations, confirming the nanoscale resolution and sensitivity of iSThM. Our studies suggest that iSThM will also allow true non-contact thermal mapping of high thermal conductivity samples. Future work may involve new probe designs tailored for iSThM, optimization of operating parameters of the probe, and development of probes capable of working in polar liquids like water or electrolytes with new biomedical and energy storage applications.

## **MATERIALS AND METHODS**

**Finite elements (FE) modeling.** The FE simulations were based on commercial COMSOL Multiphysics software package with two components, an AC/DC module modeling the current flow and Joule heating of the probe and a thermal module modeling the heat transport in the 3D probe geometry (see Supporting Material for more information). FE models were tested by varying mesh dimensions and the size of the cell, with results varying by less than 1 % indicating the adequate FE setup. As the MFP in liquid as well as in relevant materials in the models on the order of 10-25 nm, the diffusive approximation was also appropriate<sup>31</sup>.

**Experimental setup of SThM and calibration of thermal measurements.** The SP thermal probe was calibrated on a Peltier hot/cold plate (Torrey Pines Scientific, Echo Therm model IC20) at several temperatures from room temperature to 80 °C and its electrical resistance measured. During measurements and imaging the probe was included either as a part of a voltage divider in series with the fixed resistor, or a part of Maxwell electric bridge. The probe AC signal response was calibrated using the lock-in amplifier (Stanford Research Systems SRS-830) with a small applied voltage 2V AC voltage at 91 kHz for detection but small enough not to heat the tip. The voltage excitation for all measurements was provided by the precision function generator (Keithley 3390 50 MHz arbitrary waveform generator)<sup>30</sup>. As these calibrations took place outside the AFM so there was no heating affects from the laser. All calibrations were done both in air and then in dodecane with a period for the dodecane to stabilize in temperature before each

measurement. In the measurement voltage divider mode a multimeter (Agilent 34401A 6.5 digits precision) allowed measurement of the resistance of the probe as a function of the voltage at the probe which in turn allowed us to find temperature. In the measurements, Maxwell bridge configuration, the bridge was balanced at room temperature and absence of AFM laser illumination using variable resistor and capacitors before each calibration and before imaging. The imaging was done at low set force to minimize the risk of tip damage or breaking. The setup for experimental measurements can be seen in Figure 7.



A piece cut from a rubber glove was used underneath the liquid holder to protect the AFM scanner from accidental liquid spilling, however this needed to be changed from time to time as the dodecane plasticises the rubber over the time. During scanning in liquid a higher heating voltage, about 7 V<sub>DC</sub> and 3V<sub>pp</sub> AC had to be applied in order to compensate higher heat dissipation in the liquid. This allowed to reach probe temperature similar to one obtained during the operation in air. Force setpoint was kept low and the scanning rate was 0.5 Hz for most operations with the lock-in response set to 3 ms. Some care should be exercised while working underliquid as the dodecane refracted the laser beam making positioning on the beam on the cantilever difficult. The cantilevers bases were smodified so that they were tilted at a slightly shallower angle as to reflect the AFM laser back into the photodiode. The laser was aligned after



the immersion in liquid and deflection zeroed at several points during the operation underliquid, including just before tip approach.

**Samples preparation.** ULSI interconnects were cleaned by 10 min sonication consecutively in acetone, ethanol, and DI water, and finally plasma cleaned in O<sub>2</sub>/Ar plasma for 5 minutes to remove any residual organic contaminants on the surface. The graphene flake was deposited on Si wafer with 300 nm of SiO<sub>2</sub> thermal oxide that allowed the graphene to be seen in an optical microscope for area identification. The wafer was cleaned similar to the ULSU sample. The graphene was produced by mechanical exfoliation from graphite flakes using pressure sensitive tape.<sup>51</sup> The final exfoliation was done by cross-linked polymer gel (Gel-Pak, USA) to minimize tape residue transfer.

*Acknowledgments:* Authors acknowledge input of Manuel Pumarol for advice, scientific discussions and support related to the variety of aspects of SThM operation. We would like to thank Riccardo Mazzocco for his help with some of the paper's illustrations. We are also grateful to Hubert Pollock, Olaug Grude, and late Azeddine Hammiche for insight in using SThM, as well as Bob Jones for SEM analysis of the SP probes. OVK acknowledges support from the EPSRC grants EP/G015570/1, EPSRC-NSF grant EP/G06556X/1 and EU FP7 GRENADA and FUNPROBE grants. We would also like to thank the group that produced WSxM for their useful program for analysis of SPM images.<sup>52</sup>

*Supporting Information Available:* Finite element modeling of SThM response in air and liquid; simulation of tip-surface distance dependence and lateral resolution measurements in SThM; analysis of the dependence of heat loss to the ambient environment on geometry of the cantilever and properties of surrounding media; calibration of thermal measurements; experimental and simulation comparison between performance of DS and SP SThM probes.

#### References:

- 1 Binnig, G., Rohrer, H., Gerber, C. & Weibel, E. Tunneling through a controllable vacuum gap. *Applied Physics Letters* **40**, 178-180 (1982).
- 2 Binnig, G., Quate, C. F. & Gerber, C. Atomic force microscope. *Physical Review Letters* **56**, 930-933 (1986).

- 3     Garnaes, J., Schwartz, D. K., Viswanathan, R. & Zasadzinski, J. A. N. NANOSCALE DEFECTS IN LANGMUIR-BLODGETT-FILM OBSERVED BY ATOMIC-FORCE MICROSCOPY. *Synthetic Metals* **57**, 3795-3800, doi:10.1016/0379-6779(93)90515-x (1993).
- 4     Ferralis, N. Probing mechanical properties of graphene with Raman spectroscopy. *Journal of Materials Science* **45**, 5135-5149, doi:10.1007/s10853-010-4673-3.
- 5     Dinelli, F. *et al.* Mapping surface elastic properties of stiff and compliant materials on the nanoscale using ultrasonic force microscopy. *Philosophical Magazine A, Physics of Condensed Matter Structure Defects and Mechanical Properties* **80**, 2299-2323 (2000).
- 6     Patil, S., Martinez, N. F., Lozano, J. R. & Garcia, R. Force microscopy imaging of individual protein molecules with sub-pico Newton force sensitivity. *J. Mol. Recognit.* **20**, 516-523, doi:10.1002/jmr.848 (2007).
- 7     Gross, L., Mohn, F., Moll, N., Liljeroth, P. & Meyer, G. The Chemical Structure of a Molecule Resolved by Atomic Force Microscopy. *Science* **325**, 1110-1114, doi:10.1126/science.1176210 (2009).
- 8     Butt, H. J., Cappella, B. & Kappl, M. Force measurements with the atomic force microscope: Technique, interpretation and applications. *Surf. Sci. Rep.* **59**, 1-152, doi:10.1016/j.surfrep.2005.08.003 (2005).
- 9     Kvashnin, A. G., Sorokin, P. B. & Kvashnin, D. G. The Theoretical Study of Mechanical Properties of Graphene Membranes. *Fullerenes Nanotubes and Carbon Nanostructures* **18**, 497-500, doi:10.1080/1536383x.2010.488160.
- 10    Kolosov, O., Gruverman, A., Hatano, J., Takahashi, K. & Tokumoto, H. NANOSCALE VISUALIZATION AND CONTROL OF FERROELECTRIC DOMAINS BY ATOMIC-FORCE MICROSCOPY. *Physical Review Letters* **74**, 4309-4312, doi:10.1103/PhysRevLett.74.4309 (1995).
- 11    Kolosov, O. V. *et al.* Imaging the elastic nanostructure of Ge islands by ultrasonic force microscopy. *Physical Review Letters* **81**, 1046-1049 (1998).
- 12    Zhang, W. N., He, W. & Jing, X. L. Preparation of a Stable Graphene Dispersion with High Concentration by Ultrasound. *Journal of Physical Chemistry B* **114**, 10368-10373, doi:10.1021/jp1037443.

- 13 Lee, J., Liao, A., Pop, E. & King, W. P. Electrical and Thermal Coupling to a Single-Wall Carbon Nanotube Device Using an Electrothermal Nanoprobe. *Nano Letters* **9**, 1356-1361, doi:10.1021/nl803024p (2009).
- 14 Seol, J. H. *et al.* Two-Dimensional Phonon Transport in Supported Graphene. *Science* **328**, 213-216, doi:10.1126/science.1184014 (2010).
- 15 Paronyan, T. M., Pigos, E. M., Chen, G. G. & Harutyunyan, A. R. Formation of Ripples in Graphene as a Result of Interfacial Instabilities. *Acs Nano* **5**, 9619-9627, doi:10.1021/nn202972f (2011).
- 16 Marconnett, A. M., Yamamoto, N., Panzer, M. A., Wardle, B. L. & Goodson, K. E. Thermal Conduction in Aligned Carbon Nanotube-Polymer Nanocomposites with High Packing Density. *Acs Nano* **5**, 4818-4825, doi:10.1021/nn200847u (2011).
- 17 Georgantzinos, S. K., Giannopoulos, G. I. & Anifantis, N. K. Numerical investigation of elastic mechanical properties of graphene structures. *Materials & Design* **31**, 4646-4654, doi:10.1016/j.matdes.2010.05.036.
- 18 Williams, C. C. & Wickramasinghe, H. K. SCANNING THERMAL PROFILER. *Applied Physics Letters* **49**, 1587-1589 (1986).
- 19 Nonnenmacher, M. & Wickramasinghe, H. K. SCANNING PROBE MICROSCOPY OF THERMAL-CONDUCTIVITY AND SUBSURFACE PROPERTIES. *Applied Physics Letters* **61**, 168-170 (1992).
- 20 Majumdar, A., Carrejo, J. P. & Lai, J. THERMAL IMAGING USING THE ATOMIC FORCE MICROSCOPE. *Applied Physics Letters* **62**, 2501-2503, doi:10.1063/1.109335 (1993).
- 21 Nadler, M., Mahrholz, T., Riedel, U., Schilde, C. & Kwade, A. Preparation of colloidal carbon nanotube dispersions and their characterisation using a disc centrifuge. *Carbon* **46**, 1384-1392, doi:10.1016/j.carbon.2008.05.024 (2008).
- 22 Rosamond, M. C., Gallant, A. J., Petty, M. C., Kolosov, O. & Zeze, D. A. A Versatile Nanopatterning Technique Based on Controlled Undercutting and Liftoff. *Advanced Materials* **23**, 5039-5044, doi:10.1002/adma.201102708 (2011).
- 23 Majumdar, A. Scanning thermal microscopy. *Annu. Rev. Mater. Sci.* **29**, 505-585 (1999).
- 24 Choi, E. K., Jeon, I. Y., Oh, S. J. & Baek, J. B. "Direct" grafting of linear macromolecular "wedges" to the edge of pristine graphite to prepare edge-functionalized

- graphene-based polymer composites. *Journal of Materials Chemistry* **20**, 10936-10942, doi:10.1039/c0jm01728k.
- 25 Kroto, H. W., Heath, J. R., O'Brien, S. C., Curl, R. F. & Smalley, R. E. C-60 - BUCKMINSTERFULLERENE. *Nature* **318**, 162-163 (1985).
  - 26 Yang, D. J. *et al.* Thermal conductivity of multiwalled carbon nanotubes. *Physical Review B* **66**, doi:10.1103/PhysRevB.66.165440 (2002).
  - 27 van der Zande, A. M. *et al.* Large-Scale Arrays of Single-Layer Graphene Resonators. *Nano Letters* **10**, 4869-4873, doi:10.1021/nl102713c.
  - 28 Blackberg, L., Ringbom, A., Sjostrand, H. & Klintenberg, M. Assisted self-healing in ripped graphene. *Physical Review B* **82**, doi:10.1103/PhysRevB.82.195434.
  - 29 Golberg, D. *et al.* Recent Advances in Boron Nitride Nanotubes and Nanosheets. *Israel Journal of Chemistry* **50**, 405-416, doi:10.1002/ijch.201000049.
  - 30 Chen, D., Tang, L. H. & Li, J. H. Graphene-based materials in electrochemistry. *Chemical Society Reviews* **39**, 3157-3180, doi:10.1039/b923596e.
  - 31 Pumarol, M. E. *et al.* Direct Nanoscale Imaging of Ballistic and Diffusive Thermal Transport in Graphene Nanostructures. *Nano Letters* **DOI: 10.1021/nl3004946**, doi:10.1021/nl3004946 (2012).
  - 32 Pollock, H. M. & Hammiche, A. Micro-thermal analysis: techniques and applications. *Journal of Physics D-Applied Physics* **34**, R23-R53 (2001).
  - 33 Tsukruk, V. V., Gorbunov, V. V. & Fuchigami, N. Microthermal analysis of polymeric materials. *Thermochim. Acta* **395**, 151-158 (2003).
  - 34 Pylkki, R. J., Moyer, P. J. & West, P. E. SCANNING NEAR-FIELD OPTICAL MICROSCOPY AND SCANNING THERMAL MICROSCOPY. *Jpn. J. Appl. Phys. Part 1 - Regul. Pap. Short Notes Rev. Pap.* **33**, 3785-3790 (1994).
  - 35 Dobson, P. S., Weaver, J. M. R., Mills, G. & Ieee. in *2007 Ieee Sensors, Vols 1-3 IEEE Sensors* 708-711 (Ieee, 2007).
  - 36 Tsuji, T. *et al.* Evaluation of domain boundary of piezo/ferroelectric material by ultrasonic atomic force microscopy. *Jpn. J. Appl. Phys. Part 1 - Regul. Pap. Short Notes Rev. Pap.* **43**, 2907-2913, doi:10.1143/jjap.43.2907 (2004).

- 37 Hinz, M., Marti, O., Gotsmann, B., Lantz, M. A. & Durig, U. High resolution vacuum scanning thermal microscopy of HfO<sub>2</sub> and SiO<sub>2</sub>. *Applied Physics Letters* **92**, 3, doi:04312210.1063/1.2840186 (2008).
- 38 Puyoo, E., Grauby, S., Rampnoux, J. M., Rouviere, E. & Dilhaire, S. Thermal exchange radius measurement: Application to nanowire thermal imaging. *Review of Scientific Instruments* **81**, doi:10.1063/1.3455214.
- 39 Shi, L., Plyasunov, S., Bachtold, A., McEuen, P. L. & Majumdar, A. Scanning thermal microscopy of carbon nanotubes using batch-fabricated probes. *Applied Physics Letters* **77**, 4295-4297 (2000).
- 40 Chou, T. W., Gao, L. M., Thostenson, E. T., Zhang, Z. G. & Byun, J. H. An assessment of the science and technology of carbon nanotube-based fibers and composites. *Composites Science and Technology* **70**, 1-19, doi:10.1016/j.compscitech.2009.10.004.
- 41 Shi, L. & Majumdar, A. Thermal transport mechanisms at nanoscale point contacts. *Journal of Heat Transfer-Transactions of the Asme* **124**, 329-337, doi:10.1116/1.1447939 (2002).
- 42 Hu, H. W. & Chen, G. H. Electrochemically Modified Graphite Nanosheets and Their Nanocomposite Films with Poly(vinyl alcohol). *Polymer Composites* **31**, 1770-1775, doi:10.1002/pc.20968.
- 43 Geringer, V. *et al.* Intrinsic and extrinsic corrugation of monolayer graphene deposited on SiO(2). *Physical Review Letters* **102**, doi:07610210.1103/PhysRevLett.102.076102 (2009).
- 44 Putman, C. A. J., Vanderwerf, K. O., Degrooth, B. G., Vanhulst, N. F. & Greve, J. TAPPING MODE ATOMIC-FORCE MICROSCOPY IN LIQUID. *Applied Physics Letters* **64**, 2454-2456, doi:10.1063/1.111597 (1994).
- 45 Geer, R. E., Kolosov, O. V., Briggs, G. A. D. & Shekhawat, G. S. Nanometer-scale mechanical imaging of aluminum damascene interconnect structures in a low-dielectric-constant polymer. *Journal of Applied Physics* **91**, 4549-4555 (2002).
- 46 Zabel, H. Phonons in layered compounds. *Journal of Physics-Condensed Matter* **13**, 7679-7690, doi:10.1088/0953-8984/13/34/313 (2001).

- 47 Barrat, J. L. & Chiaruttini, F. Kapitza resistance at the liquid-solid interface. *Mol. Phys.* **101**, 1605-1610, doi:10.1080/0026897031000068578 (2003).
- 48 Hofbauer, W., Ho, R. J., Hairulnizam, R., Gosvami, N. N. & O'Shea, S. J. Crystalline structure and squeeze-out dissipation of liquid solvation layers observed by small-amplitude dynamic AFM. *Physical Review B* **80**, doi:10.1103/PhysRevB.80.134104 (2009).
- 49 Cahill, D. G. *et al.* Nanoscale thermal transport. *Journal of Applied Physics* **93**, 793-818, doi:10.1063/1.1524305 (2003).
- 50 Koh, Y. K., Bae, M. H., Cahill, D. G. & Pop, E. Heat Conduction across Monolayer and Few-Layer Graphenes. *Nano Letters* **10**, 4363-4368, doi:10.1021/nl101790k (2010).
- 51 Janovjak, H., Struckmeier, J. & Muller, D. J. Hydrodynamic effects in fast AFM single-molecule force measurements. *Eur. Biophys. J. Biophys. Lett.* **34**, 91-96, doi:10.1007/s00249-004-0430-3 (2005).
- 52 Horcas, I. *et al.* WSXM: A software for scanning probe microscopy and a tool for nanotechnology. *Review of Scientific Instruments* **78**, doi:10.1063/1.2432410 (2007).

# Nanoscale resolution scanning thermal microscopy in liquid environment

SUPPORTING INFORMATION.

*Peter D. Tovee and Oleg V. Kolosov.*

Physics Department, Lancaster University, Lancaster, LA1 3BE, UK.

**Finite element modeling of SThM response in air and liquid.** Finite element analysis (FE) using COMSOL Multiphysics was used for both exploring the feasibility of the immersion SThM (iSThM) idea, and, after such feasibility was experimentally confirmed, for comparison of SThM response of Al/BCB and graphene/SiO<sub>2</sub> for in-air and iSThM images. The simulation consisted of two parts; an electrical model responsible for the electric current flow in the probe, and a thermal module dealing with the Joule heating and heat propagation through the system. A fixed potential of 0.5 V was applied to the terminals of Pd heater with all other boundaries set to be electrically insulating. The thermal module used Fourier diffusive heat equations for thermal transport in material and Joule heating in the tip. As described elsewhere<sup>1</sup> due to minimal dimensions used in the modeling on the order of 50 nm that exceeded the mean-free-path (MFP) of heat carriers in the system, such approach was appropriate. In thermal module, all inner boundaries were assigned continuity conditions, with outer sides of the air/liquid block, the sample and base of the cantilever legs set to a fixed 293 K ambient temperature. With this approach the whole 3D system could be modeled and the parameters varied as desired<sup>2</sup>. A material of the block encasing the whole cantilever and sample could be changed between air, dodecane and vacuum, the tip-surface distance and tip-sample position were also independently changeable.

**Simulation of SThM response to tip-surface distance and lateral profiles in SThM.** Due to the higher thermal conductivity of dodecane compared with air, true materials sensitive non-contact scanning with nanoscale resolution – a *holy grail* of SPM approaches, is expected to be possible. With the aid of the simulations a hovering contact of up to 25 nm was compared with the full contact and the temperature drop shown in table 1 in the manuscript. There was significant deviation of the sensor response for the contact hovering in air (45 mK) with respect to the direct solid-solid contact, whereas for liquid the temperature deviation at the same distance was only 9 mK.

Lateral resolution is a very important measure for SThM probes that has been explored experimentally and using the models in this study. Simulations for samples of Al/BCB and graphene flake/SiO<sub>2</sub> were created for both air and liquid. Temperatures were taken at intervals up to 500 nm either side of the boundary with interval spacing closer near the boundary. Due to the large difference in thermal conductivities of the two materials there was a clear transition over the border with a resolution of approximately 50 nm. For graphite flake simulations we used 100

nm thick layer of graphite similar to the experiment. Its in-plane thermal conductivity was assumed to be 1000 times larger than perpendicular to the plane.<sup>3</sup> The model consisted of a Si sample block with the graphite flake on top and the sample moved with respect to the tip. As the tip made contact with the side of the flake it was then raised up and moved across the top of the flake. This allowed us to simulate the real tip's motion and also to observe the effect of side contact with the graphite flake, which may reflect higher in-plane thermal conductivity of graphite resulting in a drop in temperature observed in figure 6c in the manuscript. In figure 6d very similar experimental results are observed. It is notable that both in the experiment and simulation we observed only minor difference in SThM signal on the top of the flake and Si sample that reflects low thermal conductivity of graphite perpendicular to the atomic planes.

**Analytical model of the heat transport in iSThM - heat transport via cantilever vs heat losses to the ambient environment.**

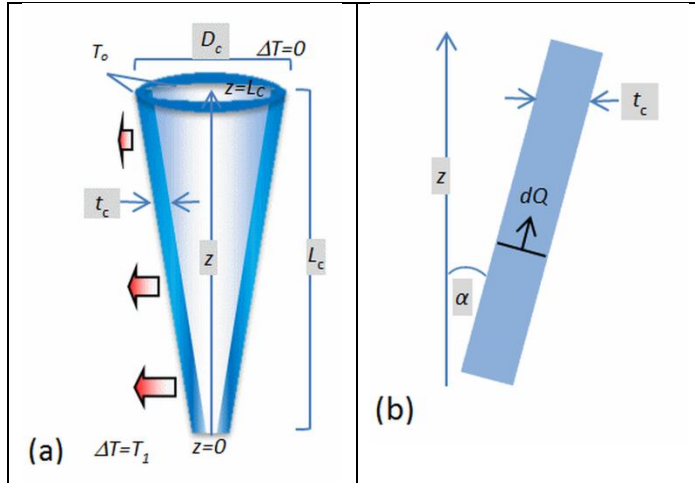


Figure S1. Equivalent analytical model of SThM sensor. (a) Schematics of the axi-symmetrical equivalent of the SP SThM probe. (b) Radial cross-section of the cantilever,  $t_c$  cantilever thickness,  $L_c$  length of the cantilever triangular section,  $\pi D_c$  – length of the base of triangular section,  $T_0$  room temperature,  $\alpha$  the cone angle and  $Q$  the heat flux down the cone wall.

As mentioned in the paper, a flat triangular geometry of the end section of the probe, fixed  $T$  at its base (close to ambient temperature due to Au leads acting as a heatsink), and evenly distributed resistive heater-sensing element along the probe, allowed to create equivalent axisymmetric model of the probe that can be evaluated analytically. These allowed to create equivalent axially symmetrical conical shell probe, setting thickness of the cone equal to the thickness of  $\text{Si}_3\text{N}_4$  probe  $t_c$ , cone half-opening angle  $\alpha$  such that the circumference of the cone base is equal to



the width  $w_c$  of the triangular end section of the probe, and the height of the cone  $L_C$  is equal to the length of the triangular section. That gives  $\alpha = \arcsin[w_c/(2\pi L_c)]$  with  $\alpha$  in our case of  $19.7^\circ$  making the equivalent geometry shaped as a narrow angle cone.

At first we calculate the thermal resistance to the base of the cantilever in a vacuum where heat is transported exclusively through the cantilever. We note that the heater in the original sensor has approximately constant width along the sensor height<sup>4</sup>, resulting in constant heating per unit height of its equivalent cone. Defining  $z$  as position along the cone with 0 at the tip and  $L_C$  at the base of the triangle, the heat generated from  $z = 0$  to  $z$  can be written as  $Q_z = zQ/L_C$ , where  $Q$  is the total Joule heat generated in the probe. This heat flows through the ring-shaped cross-section of the cone with the area  $2\pi z(\tan \alpha)t_c$  where  $t_c$  is the cantilever thickness creating heat flux

$$\frac{Q_z}{2\pi z L_C (\tan \alpha) t_c} = \frac{Q}{2\pi L_C (\tan \alpha) t_c}. \quad \text{This heat generates a temperature gradient}$$

$$\frac{dT}{dz} = \frac{1}{k_c} \frac{Q}{2\pi L_C (\sin \alpha) t_c}, \quad \text{where } k_c \text{ is the thermal conductivity of the cantilever. One can note that}$$

the temperature gradient does not depend on  $z$  and therefore is constant along the cantilever, with the temperature difference between cantilever tip and its base  $\Delta T = \frac{1}{k_c} \frac{Q}{2\pi L_C (\sin \alpha) t_c}$ . This

conclusion is very similar to the FEA simulations for the original 3D geometry of the SP SThM probe we have done in our previous work<sup>2</sup> showing approximately linear drop of the temperature along the triangular section of the SThM cantilever, therefore supporting approximations we used in this analytical model. The corresponding thermal resistance of the cantilever flux to the base is then

$$R_b = \frac{\Delta T}{Q} = \frac{1}{2\pi t_c k_c \sin \alpha} \quad (1)$$

We can also estimate the heat transport through the ambient environment (air or liquid) by considering the cone as a series of sections dissipating the heat to the environment. The flux per unit area emitted by the section of the cone at position  $z$  with section diameter  $d = 2z \tan(\alpha)$  and height  $dz$  can be estimated by assuming that it is similar to the flux from the sphere of same diameter. Although such consideration is clearly an approximation, it will allow us to compare the various components of heat transport in iSThM. The total heat flux from such a sphere to the

media per unit area is  $Q_m = \frac{2T_z k_m}{d}$  where  $k_m$  is the heat conductivity of the media<sup>5</sup>. The section

of the cone has the area on both sides of the cone  $dA = 2\pi d \frac{dz}{\cos \alpha}$ , producing flux

$$dQ_m = \frac{2T_z k_m}{d} \frac{2\pi d}{\cos \alpha} dz = \frac{4\pi T_z k_m}{\cos \alpha} dz. \text{ We can see that the heat flux to the media per unit distance}$$

along the cone (cantilever) is independent on the position  $z$  (one can note that the increase of the area losing heat was compensated by the lower heat loss efficiency per unit area for the section with the larger diameters) and depends solely on the local temperature  $T_z$ . Assuming that in each section the heat flow through the cantilever to the base dominates, we can assume the linear temperature dependence as a function of  $z$ . Then  $T_z = \Delta T (L_C - z)/L_C$  and integrating  $dQ$  over  $z$

from 0 to  $L_C$ , we obtain that the heat flux  $Q = \Delta T \frac{2\pi k_m L_C}{\cos \alpha}$  and the corresponding thermal resistance

$$R_m = \frac{\cos \alpha}{2\pi k_m L_C} \quad (2)$$

It is useful also to find a ratio of thermal resistances to the medium  $R_m$  to thermal resistance to

the base  $R_b$  by  $R_m/R_b = \frac{2\pi t_c k_c \cos \alpha \sin \alpha}{2\pi k_m L_C} = \sin \alpha \cos \alpha \frac{t_c}{L_C} \frac{k_c}{k_m}$ . This value is dimensionless and

indicates that the share of the heat flux to the media (inverse to the corresponding thermal resistance) is linearly increased with both the length of the cantilever and the heat conductivity of the media. Combining equations (1) and (2) together we can estimate the total thermal resistance  $R_t$  to the base using law of parallel resistances<sup>6,7</sup> as  $R_t = R_b R_m / (R_b + R_m)$ .

It should be noted that if the heat losses to the ambient environment started to dominate, the result will be a sharper drop of temperature with increase of distance from the tip apex. This, in turn, would additionally concentrate the heat nearer to the tip apex, that would lead to increase of the iSThM spatial resolution.

**Experimental and simulation comparison between performance of dopped Si (DS)<sup>8</sup> and Si<sub>3</sub>N<sub>4</sub> with resistive Pd sensor (SP)<sup>4</sup> probes.** Before the Si<sub>3</sub>N<sub>4</sub> SThM probes were selected as iSThM probes, two other types of probes were investigated. Initially Wollaston wire (WW) probes were used to test the validity of scanning in liquid since WW probes are more robust.

They were immersed in liquid and used on a sample of few tens of nm exfoliated graphite flakes on the glass slide. It was found that WW had not only a poor resolution due to the probe's large tip contact area, but, more essential, thermal response dominated by the overall probe distance to the sample surface, rather than sample thermal properties. The microfabricated doped Si (DS) probes (Anasys Instruments, USA) were also tested in a modified Topometrix and in Multimode AFM (Bruker, Germany) using an underliquid cell capable of holding the thermal probes. The DS probes were used with the multi-mode system to image graphene flake on glass, and an image of this can be seen in figure S3.

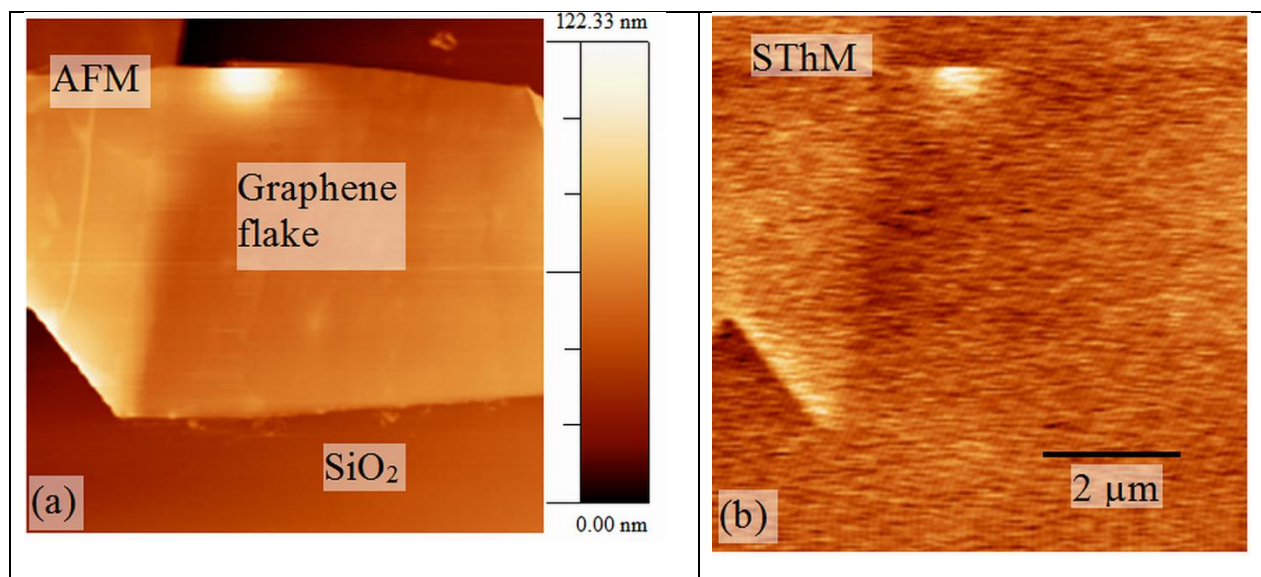


Figure S3. SThM of graphene on glass in liquid using the DS probe showing (a) AFM height image and (b) thermal image.

It is clear from figure S3 that the DS probe was also not sensitive to the change in thermal conductivity between the graphene and glass, but reflecting mainly topographical changes rather than thermal properties of the sample. This made us to conclude that the thermal sensor positioned at the end of the cantilever and far from the tip apex is detrimental to iSThM operation, while its operation in vacuum could be quite successful<sup>9</sup>. The SP probes which have their heater much closer to the tip apex and therefore the sample surface turned out to be far more sensitive to the changes in surface thermal conductivity in iSThM and therefore are preferred way for thermal scanning in liquids. We believe that future designs of optimal SThM

probes, should have similar design, that may include compatible materials allowing to operate in polar liquids such as water or electrolytes.

- 1 Majumdar, A., Carrejo, J. P. & Lai, J. THERMAL IMAGING USING THE ATOMIC FORCE MICROSCOPE. *Applied Physics Letters* **62**, 2501-2503, doi:10.1063/1.109335 (1993).
- 2 Chen, D., Tang, L. H. & Li, J. H. Graphene-based materials in electrochemistry. *Chemical Society Reviews* **39**, 3157-3180, doi:10.1039/b923596e.
- 3 Slack, G. A. ANISOTROPIC THERMAL CONDUCTIVITY OF PYROLYTIC GRAPHITE. *Physical Review* **127**, 694-&, doi:10.1103/PhysRev.127.694 (1962).
- 4 Dobson, P. S., Weaver, J. M. R., Mills, G. & Ieee. in *2007 Ieee Sensors, Vols 1-3 IEEE Sensors* 708-711 (Ieee, 2007).
- 5 Zhang, C., Breedon, M., Wlodarski, W. & Kalantar-Zadeh, K. in *Complex Systems II Vol. 6802 Proceedings of the Society of Photo-Optical Instrumentation Engineers (Spie)* (eds D. Abbott *et al.*) 80213-80213 (Spie-Int Soc Optical Engineering, 2008).
- 6 Majumdar, A. Scanning thermal microscopy. *Annu. Rev. Mater. Sci.* **29**, 505-585 (1999).
- 7 Pumarol, M. E. *et al.* Direct Nanoscale Imaging of Ballistic and Diffusive Thermal Transport in Graphene Nanostructures. *Nano Letters* **DOI: 10.1021/nl3004946**, doi:10.1021/nl3004946 (2012).
- 8 King, W. P. & Goodson, K. E. Thermal writing and nanoimaging with a heated atomic force microscope cantilever. *Journal of Heat Transfer-Transactions of the Asme* **124**, 597-597, doi:10.1115/1.1502634 (2002).
- 9 Hinz, M., Marti, O., Gotsmann, B., Lantz, M. A. & Durig, U. High resolution vacuum scanning thermal microscopy of HfO<sub>2</sub> and SiO<sub>2</sub>. *Applied Physics Letters* **92**, 3, doi:043122  
10.1063/1.2840186 (2008).